

## Silicon mirrors and micromirror arrays for spatial laser beam modulation

Steffen Kurth \*, Ramon Hahn, Christian Kaufmann, Kersten Kehr, Jan Mehner, Udo Wollmann, Wolfram Dötzel, Thomas Gessner

*Technical University Chemnitz-Zwickau, Department of Electrical Engineering and Information Technology, D-09107 Chemnitz, Germany*

Received 7 October 1997; accepted 18 November 1997

### Abstract

This contribution deals with the design, technology and experimental investigations of mirrors and micromirror arrays made of monocrystalline silicon. Electrostatically operated two-directionally deflecting mirrors and mirror arrays for continuous scanning with working frequencies between several 100 Hz and 200 kHz are presented. The modified BESOI technology used and the experimental-data-based method to improve the accuracy of model parameters for simulations and to determine the cross-coupling between array cells are new in the field of micromechanics. Furthermore, results of application-related experiments of laser projection are given. © 1998 Elsevier Science S.A. All rights reserved.

*Keywords:* Micromirror arrays; Two-directional deflection; Modified BESOI technology

### 1. Introduction

Various movable optical mirrors made of metal [1,2], polycrystalline silicon [3,4] or monocrystalline silicon [5,6] as mechanical material have been presented in the last few years. Technological approaches for monocrystalline micromirror arrays have been proposed [6]. This paper will describe the design of mirrors and mirror arrays with polished light-reflecting surfaces and electrode gaps down to 3  $\mu\text{m}$ . It includes results of simulation improvement and the experimental analysis of intercellular coupling within mirror arrays, a field with hardly any published material.

Application-dependent requirements concerning light-deflecting devices often include a relatively large optical active area of a few square millimetres, a high mechanical tilting angle up to 10° and upper working frequencies in the range of 100 Hz to several hundred kilohertz. In this case, the drawback of electrostatically operated tilting mirrors is the high driving voltage of up to 1000 V because of the mechanically necessary large electrode gap and high mass moment of inertia due to the size of the mirror plate. Generally, two approaches have been pursued. When operating at or close to the resonance frequency in order to magnify the amplitude nearly by the quality factor, the actuator performs a harmonic oscillation. Dividing the optically active area into smaller

parts, however, allows a micromirror array to be built up with a smaller electrode gap and less mass moment of inertia. Smaller dimensions lead to higher natural frequencies, large tilting angles, lower driving voltages and less translatory deflection, as shown in Fig. 1. However, the reduced optical area of the mirror cell may turn out to be a disadvantage for some applications. Micromirror arrays consisting of several small mirror cells provide a large optical area combined with the advantages of small mirror cells.

### 2. Principle of operation

The bulk-micromachined KOH-etched mirrors and mirror arrays (Fig. 2) consist of 30  $\mu\text{m}$  thick silicon plates, evaporated with reflectivity increasing metal (Al or CrAu) and suspended by silicon beams in a frame or in a mesh grating in the case of an array. The size of the light-reflecting area of the mirror or of each mirror cell is 3000  $\mu\text{m} \times 3000 \mu\text{m}$  with an electrode gap of 370  $\mu\text{m}$ .

The 5  $\mu\text{m}$  thick mirror plates and elastic beams of the micromirror arrays in modified BESOI technology (Fig. 3) contain a reflecting part on each mirror 50  $\mu\text{m} \times 250 \mu\text{m}$  in size. The size of the electrode gap is 3  $\mu\text{m}$ .

Six degrees of freedom exist assuming the mirror plate as a rigid body. Practically, only two degrees of freedom have to be taken into account when predicting the behaviour of one actuator cell. The first mode shape is the rotation of the

\* Corresponding author. Tel.: +49 371 531 32 20; fax: +49 371 531 32 59.

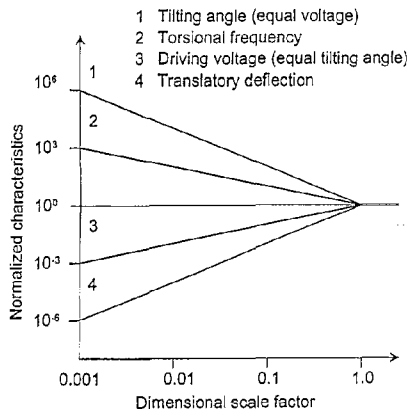


Fig. 1. The influence of dimensions on mirror properties.

moving plate. The electrical force produces an additional, in some cases undesired, translatory deflection of the mirror, which is directed to the driving electrodes. The amplitude of

the movement in further degrees of freedom is often very small and should be neglected to simplify the calculations.

Eq. (1) describes the model of a single mirror cell (see Fig. 4) as a resonator with two degrees of freedom:

$$\begin{pmatrix} J & 0 \\ 0 & m \end{pmatrix} \begin{pmatrix} \frac{\partial^2 \alpha}{\partial t^2} \\ \frac{\partial^2 w}{\partial t^2} \end{pmatrix} + \begin{pmatrix} c_r & 0 \\ 0 & c_t \end{pmatrix} \begin{pmatrix} \frac{\partial \alpha}{\partial t} \\ \frac{\partial w}{\partial t} \end{pmatrix} + \begin{pmatrix} k_r & 0 \\ 0 & k_t \end{pmatrix} \begin{pmatrix} \alpha \\ w \end{pmatrix} = \begin{pmatrix} u_{b1} \\ u_{b2} \end{pmatrix} \begin{pmatrix} e_{r1} & -e_{r2} \\ e_{t1} & e_{t2} \end{pmatrix} \begin{pmatrix} \tilde{u}_1 \\ \tilde{u}_2 \end{pmatrix} \quad (1)$$

with the mass moment of inertia  $J$ , the mass  $m$ , the damping coefficients  $c_r$  and  $c_t$ , the electrostatic coupling coefficients  $e_{rj}$  and  $e_{tj}$ , the bias voltages  $u_{bi}$  and the driving voltages  $\tilde{u}_i$ . The natural frequencies without damping are nearly given by

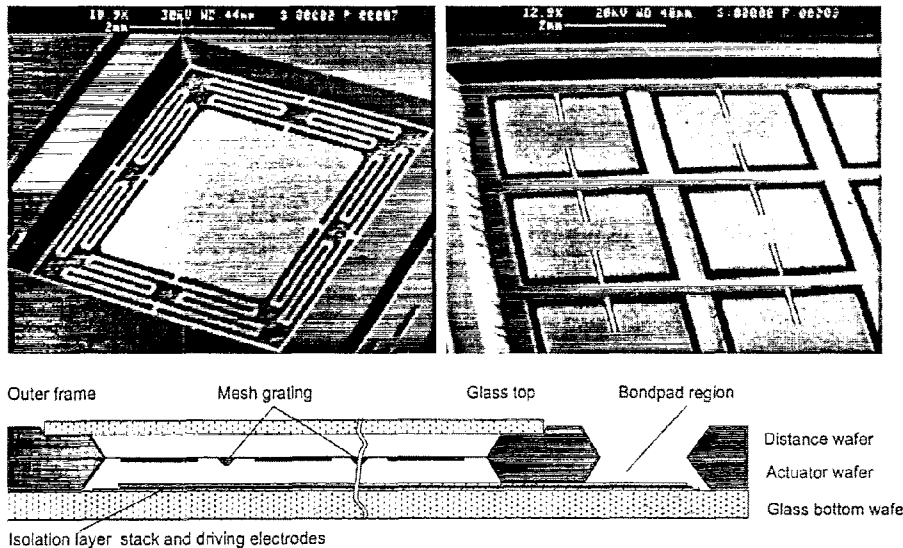


Fig. 2. SEM photograph of the back of a two-directional mirror and of a mirror array in bulk micromechanics and cross-sectional schematic view.

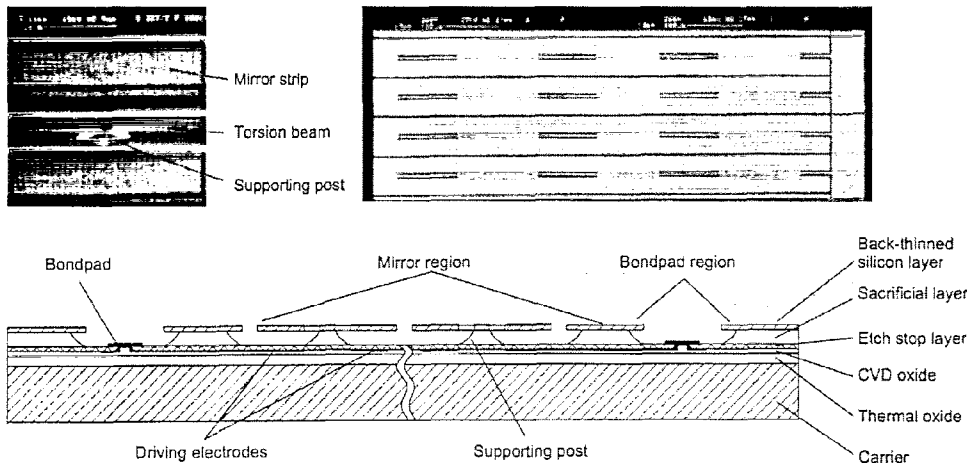


Fig. 3. SEM photographs and cross-sectional schematic view of a mirror array in modified BESOI technology.

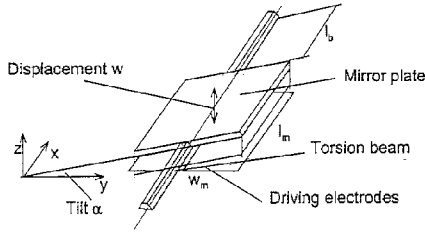


Fig. 4. Schematic of the cross section and working principle of a single cell.

$$\omega_{0r} = \sqrt{\frac{24 G_m l_t}{l_b^3 l_m w_m^3 t h \rho_{Si}}} \quad (2)$$

for rotary motion and

$$\omega_{0t} = \sqrt{\frac{24 EI}{l_b^3 l_m w_m t h \rho_{Si}}} \quad (3)$$

for translatory motion without any electrostatic field, where the shear modulus is  $G_m$ , the torsion moment is  $l_t$ , the Young's modulus is  $E$ , the area moment of inertia is  $I$ , the thickness of the silicon movable part is  $t$  and the specific weight is  $\rho_{Si}$ . The electric field of the applied bias voltage causes a displacement-dependent torque and decreases the elasticity  $k$  of the spring-mass oscillators to

$$k_r^* = k_r - \frac{d^2 C u_b^2}{d \alpha^2} \quad (4)$$

The natural frequency is decreased as well. The coefficients for electrostatic translating force and rotating torque can be expressed by

$$e_{t1} = \frac{\epsilon w_m l_m}{4d[(w_m/2)\alpha + d]} \quad (5a)$$

$$e_{t2} = \frac{\epsilon w_m l_m}{4d[-(w_m/2)\alpha + d]} \quad (5b)$$

$$e_{r1} = \frac{\epsilon l_m}{2} \left[ \frac{1}{\alpha^2} \ln \frac{d}{(w_m/2)\alpha + d} + \left( \frac{w_m/2}{(w_m/2)\alpha^2 + d\alpha} \right) \right] \quad (6a)$$

$$e_{r2} = \frac{\epsilon l_m}{2} \left[ \frac{1}{\alpha^2} \ln \frac{d}{-(w_m/2)\alpha + d} + \left( \frac{w_m/2}{(w_m/2)\alpha^2 - d\alpha} \right) \right] \quad (6b)$$

respectively, with the tilt angle  $\alpha \neq 0$  and the electrode gap  $d$ .

The damping coefficients  $c_t$  and  $c_r$ , the stiffnesses  $k_t$  and  $k_r$ , the driving force  $F_{el}$  and the driving torque  $M_{el}$  can be calculated using the finite-element method as well.

The surrounding air causes forces and moments on the mirror plate depending on the deflection and on the velocity. These forces and moments act as a mechanical damper. In some cases, if there is a significant phase lag between the plate velocity and the gas reaction force,  $\varphi_{FV}$ , the surrounding gas additionally acts as a spring ( $\varphi_{FV} > 0$ ) or as an inertial mass ( $\varphi_{FV} < 0$ ).

Most of the mechanical energy dissipates in the viscous air film within the electrode gap. If  $d \ll l_m, w_m$  and if the working frequency is less than a critical frequency  $\omega_c = \pi^2 p d^2 / 12 \eta_{eff}$

( $1/w_m^2 + 1/l_m^2$ ) [7], where  $l_m$  and  $w_m$  are lateral plate dimensions,  $p$  is the ambient pressure,  $\eta_{eff}$  is the effective viscosity [8] and  $d$  is the plate separation, no phase shift occurs. Assuming relatively small angular deflections, the ratio of gas reaction force and plate velocity can be considered as constant. Depending on the degree of freedom, these ratios describe damping coefficients of translatory and rotatory oscillations.

In the case of plates that are large compared with the electrode gap, the gas-pressure change  $P$  can be analysed by using the well-known Reynolds gas-film equation:

$$\frac{p}{12 \eta_{eff}} \left[ \frac{\partial^2}{\partial x^2} \left( \frac{P}{p} \right) + \frac{\partial^2}{\partial y^2} \left( \frac{P}{p} \right) \right] = \frac{\partial}{\partial t} \left( \frac{P}{p} \right) + \frac{w_z(x, y)}{d} \quad (7)$$

If the working frequencies are below the critical frequency  $\omega_c$ , the time-dependent term of Eq. (7) can be neglected and we get a Poisson equation, which can be readily solved for simple geometries [7].

Calculated results are:

$$c_r = \frac{M_D}{\dot{\alpha}} = \frac{\int P r dA}{\dot{\alpha}} = K_r \frac{\eta w_m^5 l_m}{d^3} \quad (8)$$

$$c_t = \frac{F_D}{\dot{w}} = \frac{\int P dA}{\dot{w}} = K_t \frac{\eta w_m^3 l_m}{d^3} \quad (9)$$

where  $A$  is the plate area,  $K_t$  and  $K_r$  depend on the aspect ratio  $l_m/w_m$  ( $K_t=0.43$  [9] and  $K_r=17.64 \times 10^{-3}$  for square plates).

If the working frequencies are above  $\omega_c$ , an analogy of Reynolds equation to the heat-transfer equation allows any plate shape and oscillation modes to be analysed with commercial finite-element tools like ANSYS. The local plate velocity must be replaced by the heat-generation rate and the temperature response has to be transformed into the pressure distribution.

In the case of large air gaps or non-free outstream conditions on the plate edges, Reynolds gas-film equation is not suitable for analysing the fluid flow. Finite-element tools with fluid-dynamic capabilities are necessary to analyse micromirror arrays separated by a suspending grid (Fig. 5). Simulations show a substantial pressure gradient outside the mirror plate. Therefore, accurate results for these structures can be found by using a time-consuming numerical fluid-flow analysis with FLOTRAN. Damping coefficients and the cross-coupling to the adjacent cells are calculated iteratively by the real part of the integrated pressure distribution on harmonic oscillating plates.

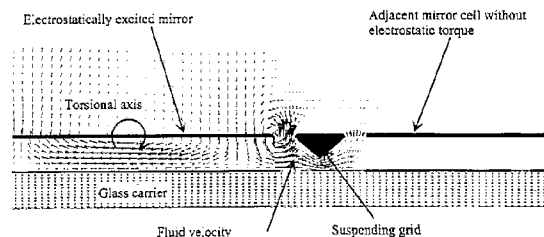


Fig. 5. Velocity plot of the fluid flow around a micromirror array using FLOTRAN.

The whole array or a part of it has to be described as numerous single cells combined with elastomechanic coupling between them, additional ‘damping’ coefficients for the fluid-dynamic coupling and further electrostatic coupling coefficients to describe the electrostatic cross-talk.

### 3. Fabrication

#### 3.1. Conventional bulk silicon mirrors and mirror array

The actuator design comprises four different wafers, a glass top wafer, an upper silicon distance wafer, a silicon actuator wafer and a glass carrier wafer. The actuator wafer and the upper distance wafer are fabricated in silicon bulk micro-machining using double-side-polished 4 inch silicon wafers. The silicon membranes situated in the actuator wafer and the frames between them are patterned by anisotropic etching with KOH using SiO<sub>2</sub> and Si<sub>3</sub>N<sub>4</sub> as etch mask. The upper distance wafer is etched anisotropically in two steps in order to define spaces for the glass cover and the mirror clearance. Silicon fusion bonding (SFB) is used to connect the silicon wafers (distance and actuator wafer). A metal (aluminium or gold) is deposited on both sides of the wafer compound using sputter masks. This layer serves as a reflector on the mirror front side and as a conducting and stress compensation layer on the mirror back side. Fabricating the glass carrier, a 150 nm Si<sub>3</sub>N<sub>4</sub> layer is deposited on the glass carrier wafer by using PECVD in order to fabricate a barrier between the glass and the driving electrodes (1 μm aluminium), which are prepared on top of the nitride. Above these electrodes, a layer stack consisting of PECVD Si<sub>3</sub>N<sub>4</sub>, PECVD SiO<sub>2</sub> and PECVD Si<sub>3</sub>N<sub>4</sub> insulates the structure against the air, since during the actuator operation a relatively high voltage is applied. The actuator wafer is attached to the glass carrier wafer by anodic bonding.

#### 3.2. Mirror array in modified BESOI technology

Following a thermal oxidation and a deposition of CVD oxide, the driving electrodes are applied on and patterned on the carrier wafer. A further CVD oxide, deposited on this wafer and on an additional blank active wafer, serves as

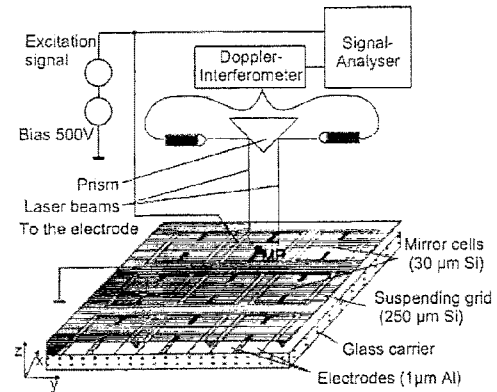


Fig. 6. Measurement set-up for the frequency response.

sacrificial layer and silicon fusion bondable surface. Before silicon fusion bonding, the wafer containing electrodes must be polished in order to remove the in-oxide-transferred electrode topology. The active wafer is thinned down to 5 μm by KOH wet etching and polished by chemical mechanical polishing. After coating the surfaces with the reflection layer and protecting them, the mirrors are structured by plasma etching and released by wet etching of the sacrificial oxide.

### 4. Characteristics

#### 4.1. Behaviour measurement

Measurement of the frequency transfer functions leads to some characteristic values: natural frequencies and damping, eigenfrequencies, d.c. transfer rates and transfer rates at a frequency near the natural frequencies. A Doppler interferometer detects the rotation concerning the x- or y-axis and the out-of-plane motion separately (Fig. 6). Statistical methods of signal processing are used to calculate the frequency response function in order to decrease the noise. Results are shown in Fig. 7 and in Table 1.

The reproducibility of the angular deflection has been tested with an electronic speckle interferometer. The position of the mirror cells was detected after switching off and on a d.c. voltage and after exciting at the resonance frequency (harmonic oscillation with 7°) with a d.c. voltage. It has been

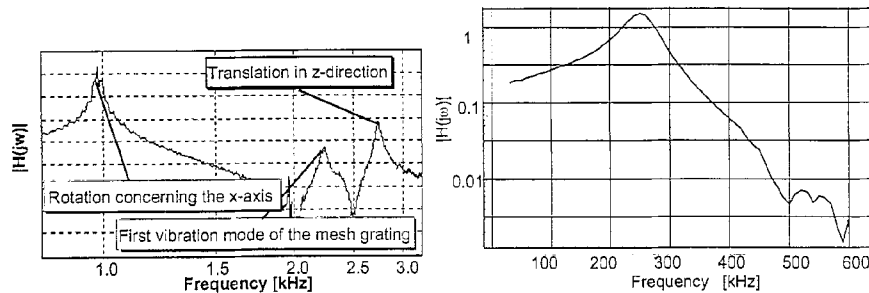






Fig. 7. Natural frequencies and mode shapes of an array in bulk micromechanics (left); frequency response function of an array in modified BESOI technology (right).

Table 1  
Results of an experimental modal analysis, natural frequencies and mode shapes

| Array in bulk micromechanics   |   | Array in modified BESOF-technology   |   |
|--|---|--|---|
| Natural frequency [Hz]   | Mode shape  | Natural frequency [Hz]   | Mode shape  |
| 994... 1020<br>1st mode<br>Rotation of the mirror plates concerning the x-axis |  | 240,000<br>1st mode<br>Rotation of the mirror plates concerning the x-axis |  |
| 2300<br>2nd mode<br>Vibration of the mesh grating                              |  |  |   |
| 2716... 2852<br>3rd mode<br>Translation of the mirror plates in z-direction    |  |  |   |

observed that the error of tilt is less than  $0.003^\circ$  according to the tilt before switching the driving voltage and before driving at the resonance frequency.

4.2. Model evaluation

One of the goals of the experimental characterization of mirrors and mirror arrays is to evaluate theoretical models describing the behaviour including the fluid, elastomechanic and electrostatic coupling mechanisms between several mirror cells and between several degrees of freedom. The matrices for inertia, damping, stiffness and force in Eq. (1) may contain appropriate parameter values (e.g., the mass moments of inertia) and, of course, more discrepant values

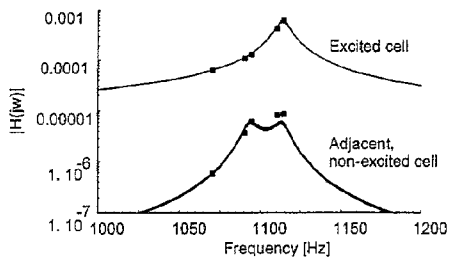


Fig. 8. Frequency response functions of an excited and an adjacent non-excited array cell, simulation data compared to the data of an experimentally enhanced model and measured data points.

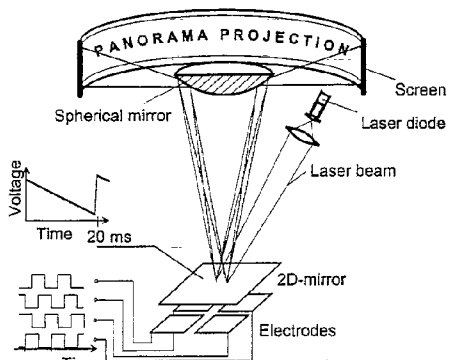


Fig. 9. Experimental set-up for pattern-scanning laser projection.

(e.g., all damping coefficients). The parameter values of the model are adapted by the method of least squares. A correction algorithm with multiple steps is used (discussed in Ref. [10]). In this way, an immediate evaluation of the calculated damping and fluid-caused coupling becomes possible. Results are shown in Fig. 8.

5. Experimental

5.1. Driving at resonance frequency

A relatively large mechanical tilting angle of up to  $10^\circ$  is achieved by driving the single 2D mirrors at the resonance frequency. The electrode voltage drives the mirror synchronously in both directions with a phase lag of  $90^\circ$  between the directions. The voltage of the mirror modulates the amplitude of the movement to scan a spiral in a plane or wind on a cylindrical screen. Modulating the laser beam intensity, a laser scanning display is accomplished. Fig. 9 shows the experimental set-up and Fig. 10 a photograph of the resulting scanning pattern.

5.2. Closed-loop control

For several applications it is suitable to operate below the resonance frequency to generate arbitrary scanning patterns. The angular deflection is of course limited by the mechanical



Fig. 10. Photograph of the screen with symbols projected by the pattern-scanning laser projection system.

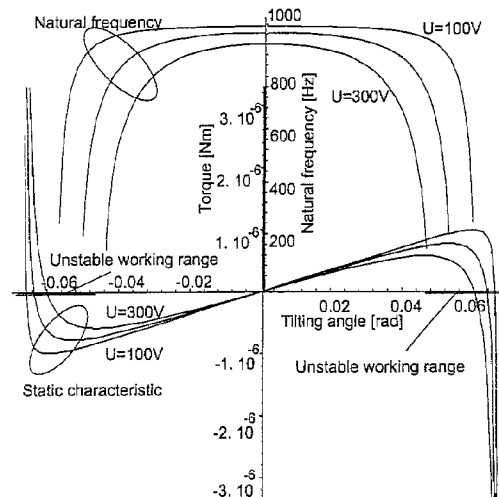


Fig. 11. Dependency of the static characteristic and natural frequency of the resonator.

# Explore Litigation Insights

Docket Alarm provides insights to develop a more informed litigation strategy and the peace of mind of knowing you're on top of things.

## Real-Time Litigation Alerts



Keep your litigation team up-to-date with **real-time alerts** and advanced team management tools built for the enterprise, all while greatly reducing PACER spend.

Our comprehensive service means we can handle Federal, State, and Administrative courts across the country.

## Advanced Docket Research



With over 230 million records, Docket Alarm's cloud-native docket research platform finds what other services can't. Coverage includes Federal, State, plus PTAB, TTAB, ITC and NLRB decisions, all in one place.

Identify arguments that have been successful in the past with full text, pinpoint searching. Link to case law cited within any court document via Fastcase.

## Analytics At Your Fingertips



Learn what happened the last time a particular judge, opposing counsel or company faced cases similar to yours.

Advanced out-of-the-box PTAB and TTAB analytics are always at your fingertips.

## API

Docket Alarm offers a powerful API (application programming interface) to developers that want to integrate case filings into their apps.

## LAW FIRMS

Build custom dashboards for your attorneys and clients with live data direct from the court.

Automate many repetitive legal tasks like conflict checks, document management, and marketing.

## FINANCIAL INSTITUTIONS

Litigation and bankruptcy checks for companies and debtors.

## E-DISCOVERY AND LEGAL VENDORS

Sync your system to PACER to automate legal marketing.